ORIGINAL RESEARCH

Layer-by-layer assembly of PDMS-coated nickel ferrite/multiwalled carbon nanotubes/cotton fabrics for robust and durable electromagnetic interference shielding

Yu Wang · Wei Wang · Qingbin Qi · Nan Xu · Dan Yu

Abstract The military and industry have multiple needs for Electromagnetic interference (EMI) shielding textiles, but it is still a huge challenge to realize integration of inorganic nanomaterials and fabric with good interface adhesion. Therefore, carefully chosen EMI materials and preparation techniques are key to provide commercially acceptable fabrics. Herein, a flexible and durable EMI shielding cotton fabric was fabricated by a layer-by-layer assembly of multi-walled carbon nanotubes (MWCNTs) and nickel ferrite ($NiFe_2O_4$) nanoparticles, following by an organic poly (dimethylsiloxane) (PDMS) coating. Benefiting from the strong interfacial interactions between MWCNTs and $NiFe_2O_4$, the efficient electrical, magnetic and thermally conductive pathways were successfully constructed on the cotton fabric. The resultant composite fabrics exhibited high electrical-magnetic properties, superior EMI shielding effectiveness of $\approx$ 84.5 dB in X-band with a 0.96 mm thickness, and markedly enhanced thermal conductivity (2.52 W m^{-1}K^{-1}). Furthermore, the external PDMS coating not only imparted a water-resistant feature, but also improved the structural and performance stability while maintaining satisfactory air permeability. Based on these results, the layer-by-layer assembly approach can be viewed as an efficient tool to fabricate protective textiles against EMI radiation pollution.

Keywords Electromagnetic interference shielding · Layer-by-layer assembly · Cotton fabric · Durability

Y. Wang · W. Wang · Q. Qi · N. Xu · D. Yu (✉)
Key Laboratory of Science and Technology of Eco-Textile, Ministry of Education, College of Chemistry, Chemical Engineering and Biotechnology, Donghua University, 2999 North Renmin Road, Songjiang District, Shanghai 201620, China
e-mail: yudan@dhu.edu.cn

W. Wang
Saintyear Holding Group Co., Ltd, Hangzhou, China

Introduction

Electromagnetic interference (EMI) shielding materials, which can block the propagation path of electromagnetic waves by reflections, absorptions and multiple reflections, are critical to resolve the problems caused by EMI radiation like undesirable damage to human beings, information security, and high precision electronic devices (González et al. 2019; Wang et al. 2019b; Xu et al. 2019). Among various EMI shielding materials, EMI shielding textiles have attracted considerable attention due to lightweight, breathable, and washable as well as high EMI shielding performance (Ghosh et al. 2018a; Huang

et al. 2016; Jia et al. 2019). Therefore, EMI shielding materials based on textiles with delicate surface design and fabrication can make them applied to all parts of the textile markets against EMI radiation pollution. Generally, textiles are intrinsically electrical insulating materials and have no EMI shielding performance (Wang et al. 2019b). Empirical research indicates that the combination of textiles and multiple inorganic materials including carbon-based materials [graphene, (Zhan et al. 2018b) carbon nanotubes (CNTs), (Zhu et al. 2019) metal carbides/nitrides (MXene) (He et al. 2019)], magnetic nanoparticles [such as Fe, (Liu et al. 2016) ferrite, (Yang et al. 2016) carbonyl iron-nickel alloy (Ren et al. 2018)], and so on (Lv et al. 2016; Zhang et al. 2016) can impart promising EMI shielding performance to them. Where these supported electrical or magnetic materials will respond to EMI radiation and then pose surface reflection and absorption of EMI waves. Despite certain EMI shielding composite materials have mushroomed nowadays, almost all studies devote to the mere improvement of EMI shielding effectiveness (SE) or these composite materials exist in the form of solid powder, (Varshney et al. 2014) films, (Li et al. 2018; Wang et al. 2019a; Zhou et al. 2018) aerogel, (Liu et al. 2018a, b) and foam, (Cui et al. 2017) it is still a formidable challenge to realize integration of multiple inorganic materials to textiles with uniform and good compatibility.

Many studies have attempted to endow textiles with excellent EMI shielding performance by electroless plating, (Hang et al. 2016) dip-coating, (Ghosh et al. 2019a, b; Liu et al. 2017b) screen printing (Huang et al. 2016) and vacuum filtration (Cataldi et al. 2017). For example, Jia et al. (2019) fabricated a highly electrically conductive fabric for ultrahigh performance EMI shielding by integrating silver nanowires and polyurethane on carbon fiber textile. Ghosh et al. (2018b) developed a conducting carbon black coated cotton fabric with a SE value of 37.7 dB. In another study, a high-performance EMI shielding textile was prepared by using collagen fiber membrane as substrate and MWCNTs-encapsulated metal nanoparticles as efficient nanofillers (Liu et al. 2017a). Note that a thick coating containing those nanofillers is usually necessary on textile to realize the target EMI SE value (20 dB) needed for commercial applications (Chen et al. 2016). Clearly, these traditional methods hinder the practical applications of their products owing to the complicate process, high cost investment, and the

impaired softness, comfort, and breathability as a textile. Furthermore, since the service environment is full of complex and diverse, the exploitation of advanced EMI shielding materials with durability in the life time and resistance to various conditions is also needed to meet the ever-growing demands. Thus, it is highly desirable to develop an efficiency strategy for constructing robust and durable EMI shielding textiles with appropriate structure while retaining the inherent properties.

Layer-by-Layer (L-b-L) assembly, namely sequential deposition of monolayers with oppositely charged nanomaterials to construct a multilayered structure, is a useful composite materials preparation method (Weng et al. 2018). Herein, this technique is very suitable for the precise construction of EMI shielding surface of textiles by controlling the building blocks and multiple L-b-L assembly cycles. To date, certain composite fabrics have been successfully fabricated by L-b-L assembly, and exhibit favorable EMI shielding performance. However, the building blocks are limited to carbon-based materials and/or conductive polymers, resulting in a lower EMI SE value (≤ 30 dB) due to the simplicity of shielding mechanism, such as (graphene oxide/polypyrrole)*n assembled wool fabric (Zou et al. 2016) and reduced graphene oxide assembled waterborne polyurethane composites (Hsiao et al. 2014). Scalable methods that can achieve the assembly of nanomaterials on textiles for further improving their EMI shielding performance while maintaining textile's intrinsic features are therefore highly needed. Among the pursued nanofillers, conductive CNTs have been regarded as one of most promising candidates for next-generation EMI shielding materials thanks to its ultrahigh electrical conductivity, low-cost and high stability (Wang et al. 2019a), while magnetic nanoparticles, like nickel ferrite ($NiFe_2O_4$), have attracted extensive attention because of their relatively high permeability and permittivity (Jiao et al. 2016; Wang et al. 2017). Following these efforts, the L-b-L assembly of conductive CNTs and magnetic $NiFe_2O_4$ nanoparticles on a textile with proper composition and structure may be an effective strategy to produce high-efficient EMI shielding textiles that possess both dielectric loss and magnetic loss. To the best of our knowledge, although carbon-based materials- and/or conductive polymer-assembled textiles have been developed for EMI shielding, effective assembly of both electrical and

magnetic components onto a textile for EMI shielding applications have not been explored so far.

In this work, an L-b-L assembled EMI shielding cotton fabric (CF) consisting of inorganic nanomaterials of MWCNTs and $NiFe_2O_4$ as dielectric-loss and magnetic-loss components, respectively was prepared and schematically described in Fig. 1a–c. Positively charged MWCNTs (P-MWCNTs) and negatively charged $NiFe_2O_4$ nanoparticles were L-b-L assembled on the outer part of MWCNTs-decorated CF and followed by the coating of organic poly (dimethylsiloxane) (PDMS) to construct an external water-resistant layer. As illustrated in Fig. 1d, the PDMS-coated $NiFe_2O_4$/MWCNTs/Cotton (PDMS/NMC)

fabric presents robust and durable EMI shielding performance thanks to the good electrical-magnetic network constructed by L-b-L assembly. In addition, the EMI shielding mechanism is also discussed in detail.

Experimental

Materials

Cotton fabric (180 g/m^2) was selected as the textile substrate and commercially available from Saintyear Holding Group Co., Ltd, China. MWCNTs powder
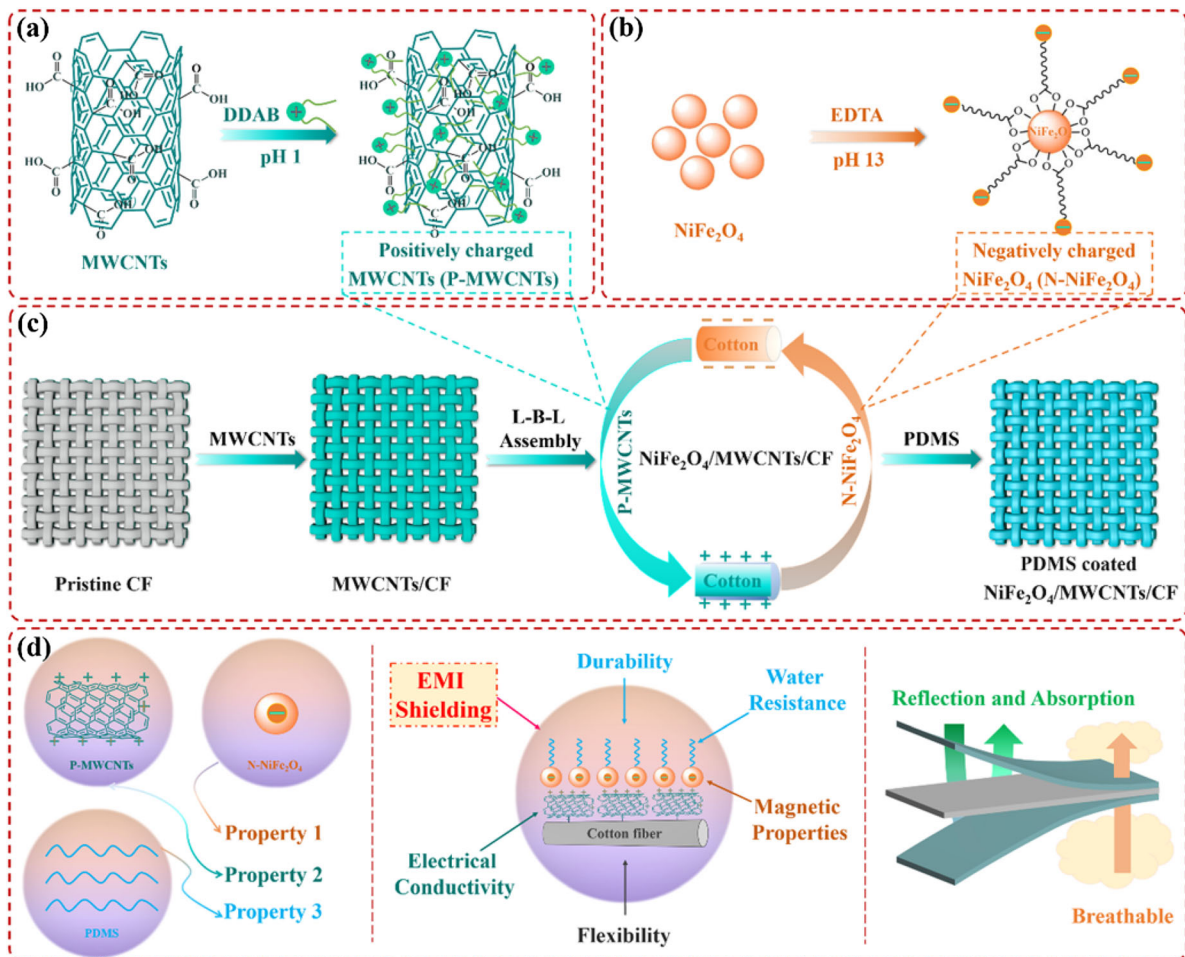
Fig. 1 Schematic illustration of the processes used to prepare the segments used in L-b-L assembly: **a** P-MWCNTs and **b** N-$NiFe_2O_4$. **c** Schematic illustrating of the fabrication of PDMS/

NMC. **d** Illustration of how this multifunctional PDMS/NMC can be designed by controlling the building components and composite structures

(average diameter < 8 nm, length 10–20 um, and purity > 98 wt%) was supplied by Beijing Boyu Gaoke New Materials Technology Co., Ltd. $NiFe_2O_4$ nanoparticles (20–30 nm) were obtained from Ashine Advanced Carbon Materials Co., Ltd, China. PDMS, ethylene diamine tetraacetic acid (EDTA), dimethyl-dioctadecylammonium bromide (DDAB), (sodium dodecylbenzene sulfonate (SDBS) and etc. were purchased from Adamas Reagent and used as received without further purification.

Preparation of P-MWCNTs and N-$NiFe_2O_4$

As illustrated in Fig. 1a, the P-MWCNTs solution was synthesized by a facile surface modification process. Briefly, to obtain uniform P-MWCNTs solution, DDAB (50 mg) was dissolved into MWCNTs aqueous solution (5 mg/mL, sonication for 1 h) and the mixture was then ultrasonicated (40 KHz) in hydrochloric acid surrounding at room temperature for 12 h. In a typical approach for fabricating N-$NiFe_2O_4$ solution, the EDTA-functionalized $NiFe_2O_4$ nanoparticles were first synthesized as presented in Fig. 1b. Specifically, $NiFe_2O_4$ nanoparticles (200 mg) and EDTA (100 mg) were dispersed into 50 ml distilled water with mechanical stirring (600 r/min) at 60 °C for 6 h, and then the product was collected by a magnetic separation. Afterwards, the uniform N-$NiFe_2O_4$ solution was obtained by dispersing the EDTA-functionalized $NiFe_2O_4$ nanoparticles into alkaline aqueous solution.

Preparation of PDMS/NMC fabrics

EMI shielding coating was L-b-L assembled on CF, as shown in Fig. 1c by selecting N-$NiFe_2O_4$ and P-MWCNTs as building blocks. Firstly, CF was treated with MWCNTs by a chemical vapor deposition method to form a negatively charged surface in order to increase the adhesion fastness between CF substrate and $NiFe_2O_4$/MWCNTs coatings to be deposited. In brief, CF (5 × 5 cm^2) and MWCNTs dispersion solution (0.2 mg MWCNTs and 0.1 g SDBS were dispersed in 50 mL distilled water) were added successively into a well-closed container, then the container was placed in an infrared-ray dyeing proofing machine and followed by holding at 130 °C (0.35 MPa pressure) for 1.5 h. Here, the driving forces for the formation of MWCNTs/Cotton fabric are due to hydrogen bonding and physical combination between

cotton fabric and MWCNTs (Fig. S1 in the supporting information). After that, the anionic MC fabric was immersed into the above P-MWCNTs solution for 3 min and dried at 80 °C for 2 min to deposit a layer of the cationic P-MWCNTs. Subsequently, the sample was dipped into the N-$NiFe_2O_4$ dispersion solution (sonication for 1 h) for 30 min and dried at 80 °C for 2 min to form negatively charged N-$NiFe_2O_4$ layer. These two deposition procedures repeated until the satisfactory magnetic-electric $NiFe_2O_4$/MWCNTs/ Cotton fabric was obtained, designated as NMC-n for convenience, where n is the number of $NiFe_2O_4$/ MWCNTs layer deposition cycles. In this process, the adhesion forces for multilayer $NiFe_2O_4$/MWCNTs formation are the electrostatic and Van Der Waals interactions between N-$NiFe_2O_4$ and P-MWCNTs. To achieve the hydrophobicity and durability, the NMC-n fabrics were immersed into a PDMS/isopropanol solution (1:50 volume ratio) for 10 s and followed were cured at 100 °C for 10 min. The resulting PDMS coated NMC-n fabrics were denoted as PDMS/NMC-n. For comparison, the PDMS coated MC (PDMS/ MC) fabric was also prepared according to the same approach.

Material characterizations

The chemical structure was characterized by a Nicolet 6700 FTIR spectra (USA). Morphological and compositional characterizations were carried out using a field-emission transmission electron microscope (FE-TEM, FEI Tecnai 20, USA) at an acceleration voltage of 200 kV, a Hitachi S4800 scanning electron microscope (SEM, USA) coupled with energy dispersive spectroscopy (EDS, Quanta250, UK). The Zeta potentials were measured by a Malvern Particle Size & Zeta Potential Analyzer (Nano S90, UK). The contact angle (CA) was recorded using a Date physics TUB 90E goniometer. Electrical conductivity was measured using a standard four-point probe surface resistance tester (MCP-T370, Japan). The hysteresis loops were characterized by a vibrating sample magnetometry (Squid-VSM, USA) at room temperature. The air permeability was recorded using air permeability tester (Model YG461E, Ningbo Textile Instrument Co. Ltd.) according to the standard for fabric air permeability (ISO 9237 − 1995) with the test area of 20 cm^2 and the pressure difference of 100

Pa. The thermal conductivity was determined using a thermal constants analyzer (Hot Disk, Sweden).

The scattering parameters (S_{11} and S_{12} or S_{21} and S_{22}), relative complex permittivity ($\epsilon_r = \epsilon' - j\epsilon''$) and complex permeability ($\mu_r = \mu' - \mu''$) were measured by an Agilent N5244A vector network analyzer in the frequency range of 8-12.4 GHz (X band) using the waveguide method. All tested samples (22.86 mm × 10.16 mm) were tightly fixed with the copper sample holder and connected between the waveguide flanges. The reflection coefficient (R) and transmission coefficient (T) are determined by S parameters (S_{11}, S_{12}, S_{21}, and S_{22}). There is a balance between R, T, and absorption coefficient (A), which can be evaluated by the following equations:(Ghosh et al. 2018b)

$$R = |S_{11}|^2 = |S_{22}|^2 \tag{1}$$

$$T = |S_{12}|^2 = |S_{21}|^2 \tag{2}$$

$$R + T + A = 1 \tag{3}$$

According to Schelkunoff's theory, the total EMI SE (SE_T) is the sum of reflection loss (SE_R) at surface, multiple reflection loss (SE_M) and absorption loss (SE_A) inside the material. SE_T is defined as the logarithmic ratio of incident power (P_I) and transmitted power (P_T) of radiation and can be expressed in the following equation:(Ren et al. 2018)

$$SE_T(dB) = -10log\left(\frac{P_T}{P_I}\right) = SE_R + SE_M + SE_A \tag{4}$$

$$\begin{aligned} SE_A(dB) &= -10log\left(\frac{S_{12}^2}{1 - S_{11}^2}\right) \\ &= -10log\left(\frac{S_{21}^2}{1 - S_{11}^2}\right) \end{aligned} \tag{5}$$

$$SE_R(dB) = -10log\left(1 - S_{11}^2\right) = -10log\left(1 - S_{22}^2\right) \tag{6}$$

The SE_M can be neglected when the $SE_T > 15dB$ and it can be described as:

$$SE_T \approx SE_R + SE_A \tag{7}$$

Results and discussion

L-b-L assembly of P-MWCNTs and N-NiFe$_2$O$_4$ on CF

Figure 1 illustrated the fabrication process of PDMS/NMC fabrics, in which MWCNTs, NiFe$_2$O$_4$, and PDMS were utilized as the major building blocks. To complete the L-b-L assembly of conductive MWCNTs and magnetic NiFe$_2$O$_4$ on the cotton matrix, the oppositely charged MWCNTs and NiFe$_2$O$_4$ were essential. In this work, DDAB, the cationic surfactant, was used to modify the MWCNTs denoted as P-MWCNTs, where the hydrophobic parts of DDAB can adsorb onto the hydrophobic basal plane of MWCNTs and the hydrophilic part exhibit the positive charges. We then used FTIR and FE-TEM to investigate the chemical structure and morphology of the as-prepared P-MWCNTs, respectively. In the FTIR spectrum of P-MWCNTs (Fig. 2a), the peaks appeared at 1488 and 1375 cm^{-1} corresponded, respectively, to C-N asymmetric stretching vibration (CH$_3$-N) and C-H stretching vibration (-CH$_3$) of DDAB, suggesting the adsorption of DDAB on the MWCNTs. Moreover, compared to the smooth MWCNTs, (Cao et al. 2012) the P-MWCNTs displayed a rougher surface with bright edges (Fig. 2b), indicating DDAB had been randomly absorbed on the MWCNTs surface as expected. In a higher-resolution FE-TEM image (Fig. 2c), it could be observed that the excessive DDAB even formed many micelles on the MWCNTs surface, which was attributed to the fact that the hydrophobic long alkyl chains of DDAB easily entangle when solvent evaporated, and thus generate globular structures. All these results revealed the successful modification of MWCNTs with DDAB. According to our previous study, (Wang et al. 2017) the NiFe$_2$O$_4$ nanoparticles could be functionalized using carboxyl group through conjugate and hydrogen bonding, therefore, we selected the EDTA with four carboxyl groups to prepare the N-NiFe$_2$O$_4$. As depicted in Fig. 1d, the FTIR spectrum of N-NiFe$_2$O$_4$ contained all characteristic peaks of NiFe$_2$O$_4$ and EDTA, implying the successful functionalization. This result was also further confirmed by the FE-TEM images (Fig. 2e and f), as the bright amorphous EDTA layer was distinctly different from the NiFe$_2$O$_4$ cores.
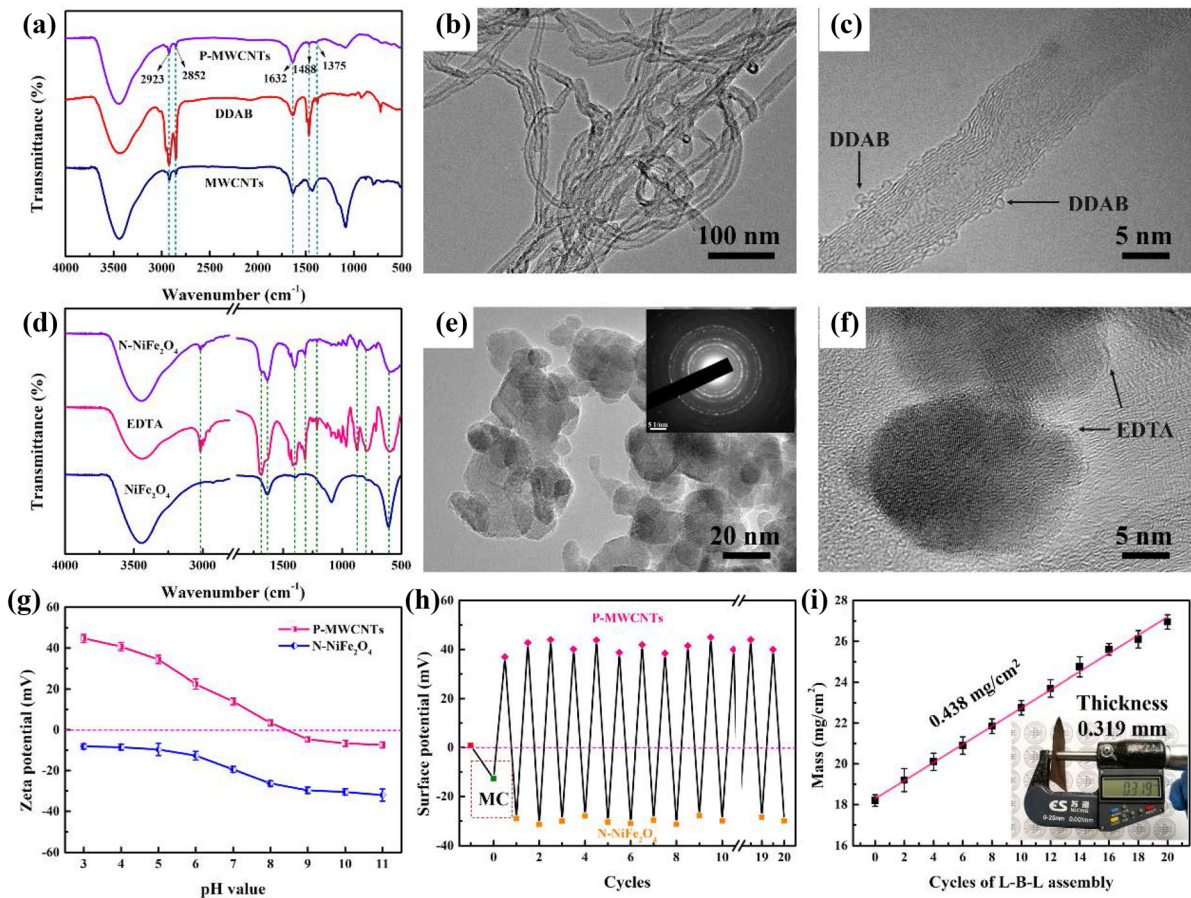
Fig. 2 a FTIR spectra of MWCNTs, DDAB, and P-MWCNTs.
b, c FE-TEM images of P-MWCNTs. d FTIR spectra of
NiFe$_2$O$_4$, EDTA, and N-NiFe$_2$O$_4$. e, f FE-TEM images of
N-NiFe$_2$O$_4$. g Zeta potentials of P-MWCNTs and N-NiFe$_2$O$_4$ as

a function of different pH values of solutions. h Surface
potentials as a function of the cycles of L-b-L assembly. i The
growth of NiFe$_2$O$_4$/MWCNTs layer expressed by the average
mass per unit area as a function of cycles of L-b-L assembly

Since the charge of P-MWCNTs and N-NiFe$_2$O$_4$
can be controlled by the degree of ionization of DDAB
and EDTA, respectively, an optimal pH value of
P-MWCNTs and N-NiFe$_2$O$_4$ solutions is critical to
obtain highly charged P-MWCNTs and N-NiFe$_2$O$_4$.
Figure 2g showed the dependence of zeta potential of
P-MWCNTs and N-NiFe$_2$O$_4$ solutions on different pH
values. Note that the zeta potential decreased gradu-
ally with increasing pH value in both P-MWCNTs and
N-NiFe$_2$O$_4$ solutions. In the case of P-MWCNTs
solution, the acidic environment reduced the
hydrophilicity of MWCNTs by inhibiting the ioniza-
tion of carboxyl groups on the MWCNTs surface,
which was propitious to the adsorption of DDAB on
the hydrophobic basal plane of MWCNTs, thus made

the zeta potential increasingly positive. As for the
N-NiFe$_2$O$_4$ solution, the alkaline environment would
increase the number of the ionized carboxylic groups
(–COO$^-$) on the NiFe$_2$O$_4$, thus the zeta potential
became increasingly negative charge with increasing
pH value. Because a sufficiently large zeta potential
difference between P-MWCNTs and N-NiFe$_2$O$_4$
would effectively facilitate L-b-L assembly, we
therefore selected the optimal pH conditions as
following: P-MWCNTs solution at pH 3 (+ 44.7
mV) and N-NiFe$_2$O$_4$ solution at pH 11 (− 32.1 mV).
To further testify the formation of NiFe$_2$O$_4$/MWCNTs
layers deposited on the CF substrate, the surface
potential of composite fabrics was also measured
(Fig. 2h). As expected, a negatively charged surface

(− 12.7 mV) was induced on the CF substrate after treatment by MWCNTs, which helped to increase the surface adhesion between CF substrate and NiFe$_2$O$_4$/MWCNTs coatings. Afterwards, the P-MWCNTs and N-NiFe$_2$O$_4$ layers were alternatively assembled on the MC fabric, which caused oscillations of the surface potentials roughly between these two potentials of oppositely charged components, suggesting that a stepwise NiFe$_2$O$_4$/MWCNTs layer growth had taken place. The average mass per unit area of NMC-n fabrics displayed a linear growth behavior (0.438 mg/cm^2 per NiFe$_2$O$_4$/MWCNTs layer) with increasing cycles of NiFe$_2$O$_4$/MWCNTs layer assembly (Fig. 2i). After 20 cycles of L-b-L assembly, the obtained NMC-20 sample presented brownish black with average thickness of 0.319 mm, indicating that the NiFe$_2$O$_4$/MWCNTs layer had been completely deposited on the CF substrate.

Morphologies and water-resistant performances of PDMS/NMC fabrics

Figure 3a–f presented the morphologies and microstructures of pristine CF, MC, and NMC-n fabrics. The pristine CF displayed a smooth surface and numerous pores among the interlaced fibers. After treatment, a thin MWCNTs film was formed on the CF surface (Fig. 3b and Fig. S1). While the NiFe$_2$O$_4$/MWCNTs layer assembled NMC-n samples exhibited rougher fiber surface conformally coated with intensive MWCNTs and tiny NiFe$_2$O$_4$ nanoparticles. Apparently, as increasing cycles of L-b-L assembly, the fiber surfaces also became rougher with large aggregated NiFe$_2$O$_4$/MWCNTs, indicating that more NiFe$_2$O$_4$/MWCNTs were wrapped on the fibers. Despite certain narrow slits were covered by the NiFe$_2$O$_4$/MWCNTs layers, the overall fabric structure was well preserved and the large pores among the intertwined fibers were not blocked after L-b-L assembly. In addition, the chemical composition and elemental distribution on the surface of NMC-20 sample revealed the uniform and continuous NiFe$_2$O$_4$/MWCNTs layers on the interconnecting fibers (Fig. 4g and Fig. S2), which would produce more perfect conducting network. The results were attributed to the strong electrostatic and Van Der Waals interactions between N-NiFe$_2$O$_4$ and P-MWCNTs, this is why a durable and uniform NiFe$_2$O$_4$/MWCNTs layer was formed on the CF.

Owing to the strong affinity between the external N-NiFe$_2$O$_4$ layer and water, the NMC samples exhibited a good hydrophilicity (Fig. S3a), however, which made NMC fabrics susceptible to contamination and/or corrosion in practical application. Therefore, it is crucial to convert the hydrophilic NMC fabrics into hydrophobic by a PDMS coating for long-term stability and self-cleaning applications. SEM image (Fig. 3h) and FTIR spectra (Fig. S3b–d) demonstrated that PDMS coating was wrapped the NMC samples surface tightly. Apparently, the surface of composite fabric after PDMS coating treatment became smoother with root mean square surface roughness values reduced from 36.1 nm to 25.5 nm. In contrast to hydrophilic NMC-20 sample, the PDMS coating covered the hydrophilic groups on NMC-20 surface and reduced the surface tension, and thus exhibited hydrophobic performance. To quantify the hydrophobic degree, the water contact angle was measured. As presented in Fig. 3i, the PDMS/NMC-20 exhibited an initial water contact angle of 139.8° and the water droplet were still well preserved within 60 s, which allow for waterproof and corrosion resistance when it was exposed to a high-humidity environment. More importantly, the satisfactory hydrophobicity also made water droplets roll off the hydrophobic surface, which can remove the adsorbed contaminants and/or dust, realizing a self-cleaning function.

Electrical, magnetic, and electromagnetic properties

The electrical, magnetic and electromagnetic properties are of major significance for EMI shielding materials, which can reflect the EMI SE value to some extent. Figure 4a presented the dependence of electrical conductivity (σ) and the numbers of L-b-L assembly cycles. Significantly, the NMC samples presented a higher electrical conductivity than its corresponding PDMS/NMC samples due to the slight detrimental effect of the insulating PDMS layer on the conductive network. In addition, the electrical conductivity of NMC and PDMS/NMC rapidly increased with increasing cycles of L-b-L assembly. Benefiting to the strong chemical bonding and physical adhesion between CF and MWCNTs, both MC and PDMS/MC samples (0 cycle of L-b-L assembly) exhibited the electrical conductivity of 1.26 and 1.13 S/m, respectively, which were higher than 1 S/m needed for
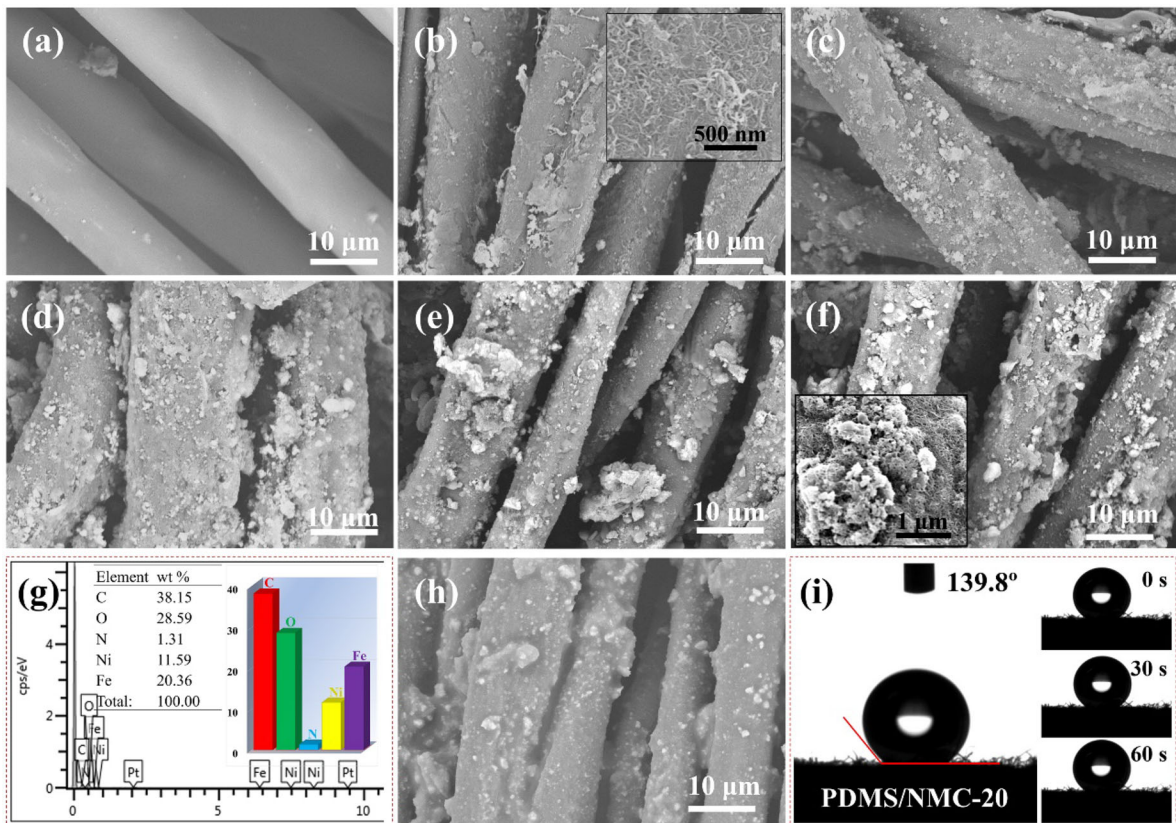
Fig. 3 SEM images of **a** pristine CF, **b** MC, **c** NMC-5, **d** NMC-10, **e** NMC-15, **f** NMC-20. **g** EDS elemental maps of NMC-20. **h** SEM image of PDMS/NMC-20. **i** Water contact angle measurements of PDMS/NMC-20

commercial applications of EMI shielding materials. Furthermore, a superior electrical conductivity of up to 18 S/m was obtained after twenty cycles, which could light up a small bulb when connected as a wire with a 12 V battery, indicating that the completely conductive network of electrical conduction had been fabricated. To endure a discretional deformation during practical applications, the conductive fabrics should possess satisfactory structural stability and mechanical flexibility. Figure 4b presented the relative surface resistance changes of NMC-20 and PDMS/NMC-20 subjected to bending and torsion tests. The as-fabricated fabrics exhibited excellent flexibility as they could be readily twisted into desirable shapes and angles. Moreover, it was worth noting that the PDMS coating markedly reduced the surface resistance change sensitivity when the sample was bent and/or twisted. In the case of NMC-20, the $NiFe_2O_4$/MWCNTs layer was liable to yield more fractures and cause apparent resistance change. But for PDMS/

NMC-20, the insulating PDMS layer effectively prevents the fractures, resulting in less resistance change. These results revealed the favorable mechanical and performance stability of PDMS/NMC-20, allowing for great applications, such as flexible electronic textiles, sensors, and EMI shielding.

As shown in Fig. 4c, the magnetic hysteresis loops presented soft magnetic behaviors with a slender S-like shape, which was helpful to obtain high EMI shielding performance.(Wang et al. 2019a) The saturation magnetization (Ms) of PDMS/NMC fabrics indicated an increasing behavior with increasing cycles of L-b-L assembly, and the PDMS/NMC-20 sample demonstrated the highest Ms value (10.3 emu/g). Meanwhile, the fact that PDMS/NMC-20 sample could be easily attracted by a magnet also revealed the excellent magnetic property. Based on these pleasant electrical-magnetic properties, a simple circuit was assembled by conductive lines, a small bulb, battery, and a switch of PDMS/NMC-20 sample (Fig. 4d). As
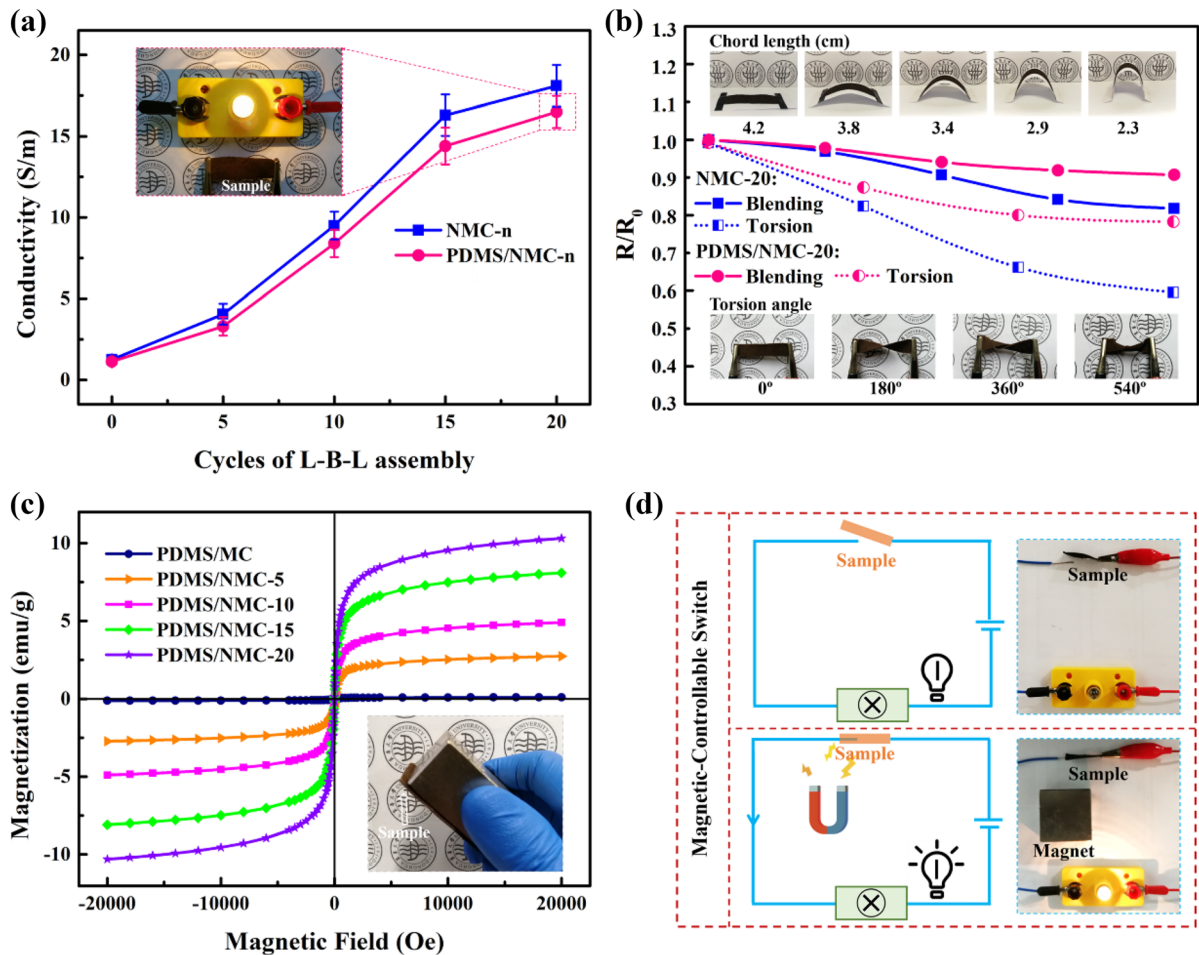
Fig. 4 a Electrical conductivity of NMC and PDMS/NMC fabrics as a function of the cycles of L-b-L assembly. b The relative surface resistance changes of NMC-20 and PDMS/NMC-20 fabrics during bending and torsion tests. c Magnetic hysteresis loops of PDMS/NMC fabrics (inset showed that the PDMS/NMC-20 sample could be attracted to a magnet easily). d The demonstration of the PDMS/NMC-20 sample used as a magnetic-controllable switch in circuit

expected, the PDMS/NMC-20 sample was driven to move closer to the magnet when a magnet was placed near it, the circuit thus was turned on and the small bulb was lightened up. Compared with reported mechanical sensors and/or magnetic metal-based switches, the electrical-magnetic PDMS/NMC-20 with favorable mechanical and performance stability were considered as a promising magnetic-controllable switch that can be applied in various circuits or other electronic devices.

Electromagnetic properties can be explained by complex permittivity and complex permeability, which determine the EMI performance of the material interacts with the electromagnetic fields. Figure 5 showed the electromagnetic properties of PDMS/

NMC-n fabrics in X-band. As seen from Fig. 5a–d, both the complex permittivity and complex permeability indicated an increasing behavior with increasing cycles of L-b-L assembly, implying the increasing dielectric loss and magnetic loss properties. For example, when the cycles of L-b-L assembly increased from 0 to 20, the real (ϵ') and imaginary (ϵ'') parts of the complex permittivity rose from 8.1–9.2 and 3.9–6.2 to 13.3–20.8 and 10.1–12.5 ranges, respectively. The obviously increasing ϵ' value was attributed to the L-b-L assembly configuration. With the increase of cycles of L-b-L assembly, the higher content of MWCNTs was added on the fabric substrate, more interfaces were formed, which doubtlessly increased the ϵ' value of such composite fabrics. While the ϵ'' of
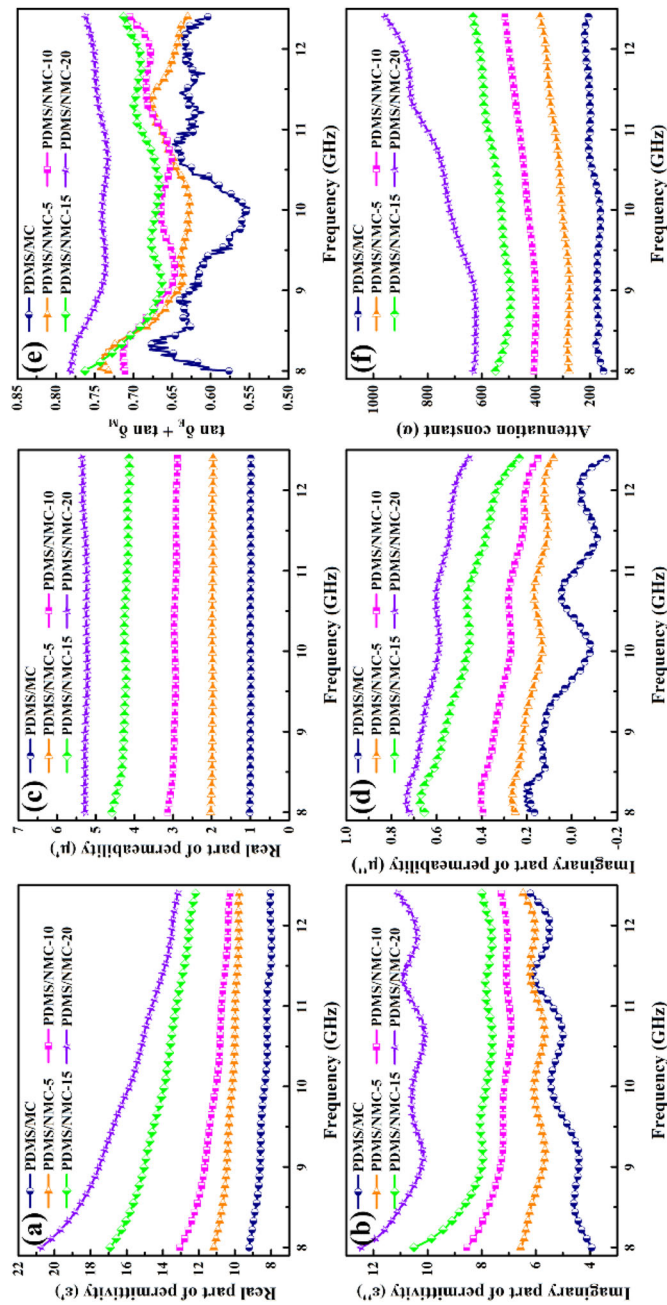
Fig. 5 Electromagnetic properties of the composite fabrics: **a** real and **b** imaginary parts of the complex permittivity, **c** real and **d** imaginary parts of the complex permeability, **e** the combined loss tangent, and **f** attenuation constant
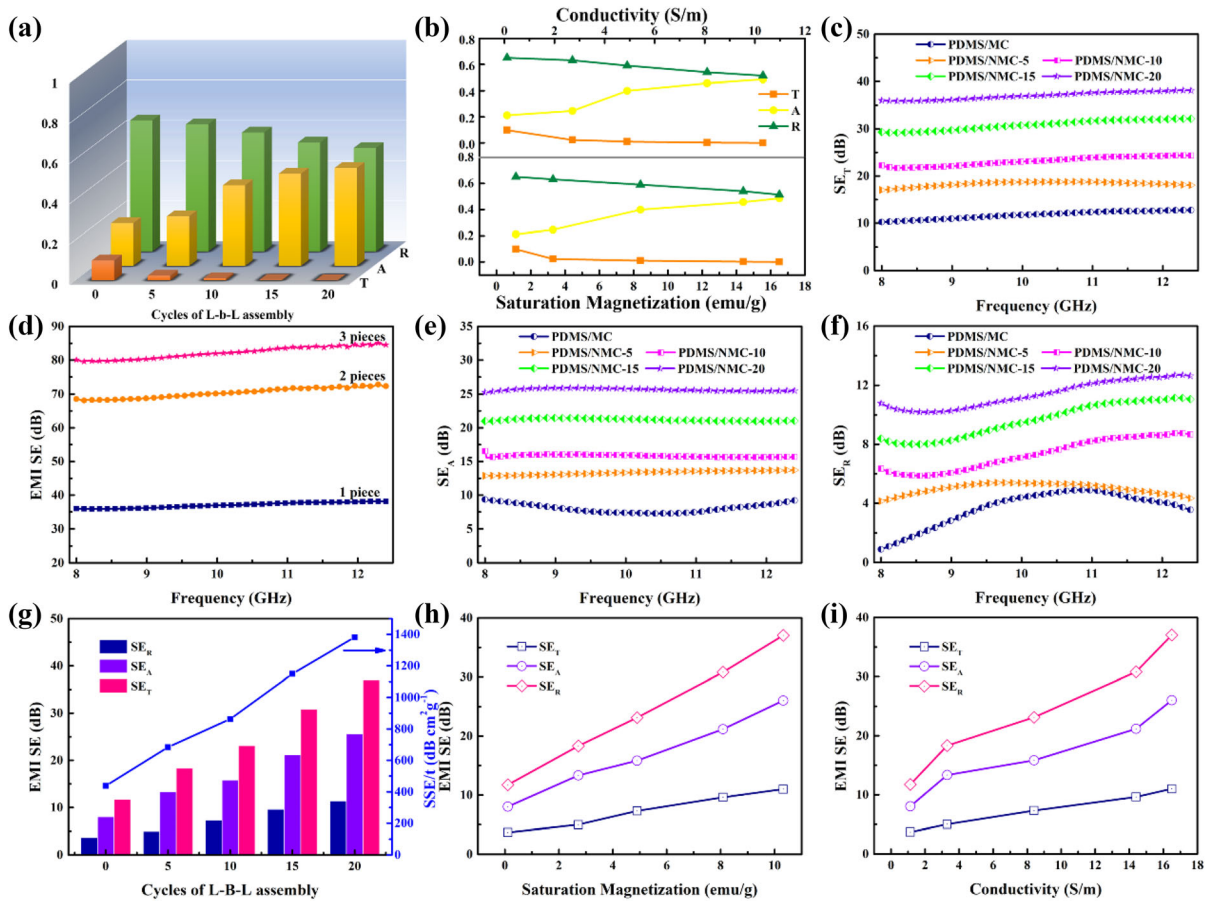
Fig. 6 **a** Average R, A, and T values of the PDMS/NMC fabrics with different cycles of L-b-L assembly in the X-band at a thickness of 0.319 mm. The EMI SE characterization setup used in this work was showed in Fig. S4. **b** Average R, A, and T values versus the electrical conductivity and saturation magnetization. Comparison of **c** SE_T, **e** SE_A and **f** SE_R of the PDMS/ NMC fabrics. **d** Effect of thickness on EMI SE for PDMS/NMC-20 fabric. **g** Average SE_T, SE_A, SE_R and specific EMI SE (SSE/t) values of the PDMS/NMC fabrics in the X-band. Average SE_T, SE_A, and SE_R values versus the **h** electrical conductivity and **i** saturation magnetization

the composite fabrics depended on the high electrical conductivity and conductive network from MWCNTs, which engendered the strong space charge polarization and electron polarization. These results confirmed that the dielectric loss properties of composite fabrics originated mainly from MWCNTs. As for the increasing complex permeability, it is accessible that the higher real (μ') and imaginary (μ'') parts of complex permeability were attributed to the strong interfacial interactions between MWCNTs and $NiFe_2O_4$, and hence conduce to higher content of $NiFe_2O_4$ was assembled on the fabric. The combined loss tangent (tan δ_E + tan δ_M = $\epsilon''/\epsilon' + \mu''/\mu'$) and attenuation constant (α) also provides a distinct understanding about the ability of microwave absorption. The larger

α value is propitious to strengthen the microwave absorption performance, and can be estimated according to the following equation:(Zhang et al. 2016)

$$\alpha = \frac{\sqrt{2}\pi f}{c} \times \sqrt{(\mu''\epsilon'' - \mu'\epsilon') + \sqrt{(\mu''\epsilon'' - \mu'\epsilon')^2 + (\epsilon'\mu'' + \epsilon''\mu')^2}}$$

(8)

where f and c are the frequency and velocity of light (3×10^8 m/s), respectively. Evidently, the increasing tan δ_E + tan δ_M and α demonstrated the capability of composite fabrics in converting the electromagnetic energy to other forms of energy grew gradually with increasing L-b-L assembly cycles (Fig. 5e, f).

Therefore, the combination of electrical/dielectric properties of MWCNTs and magnetic properties of $NiFe_2O_4$ facilitated the enhancement of EMI shielding performance.

EMI shielding performance

Generally, a good EMI shielding material must effectively attenuate the propagating electromagnetic energy mainly through the reflection and/or absorption mechanisms.(Shahzad et al. 2016) To gain a comprehensive understanding of EMI shielding properties, the reflection coefficient (R), absorption coefficient (A), and transmission coefficient (T), namely the ability of a material to reflect, absorb, and transmit electromagnetic waves, respectively, were evaluated from the S-parameters (Fig. 6a). Note that the PDMS coating did not significantly affect the EMI shielding performances of composite fabrics (Fig. S5). For the all PDMS/NMC samples, R was always larger than A, suggesting that reflection was the dominant EMI shielding mechanism. With increasing cycles of L-b-L assembly, the PDMS/NMC fabrics exhibited an incremental A and a decreasing R, which was attributed to the augments of electrical and magnetic properties (Fig. 6b). This result also demonstrated that the surface impedance matching characteristic of PDMS/NMC fabrics was improved with the increase of L-b-L assembly cycles. Furthermore, T decreased gradually from 0.0981 to $\sim 10^{-5}$ with the increase of L-b-L assembly cycles from 0 to 20; when exceeding 10 cycles, more than 99.99% of incident electromagnetic waves were shielded by the sample. As a result, our PDMS/NMC fabrics were expected to possess good surface impedance matching characteristic and EMI shielding performance by controlling the L-b-L assembly cycles.

Figure 6c–f presented the comparison of total EMI SE (SE_T), microwave absorption (SE_A) and microwave reflection (SE_R) of PDMS/NMC fabrics with different L-b-L assembly cycles in X-band. Both SE_A and SE_R contributed to the SE_T. The PDMS/MC fabric with zero-cycle assembly exhibited a poor EMI shielding performance (< 15 dB). After the L-b-L assembly, the obtained PDMS/NMC fabrics had a linear growth of EMI SE, which increased with increasing numbers of L-b-L assembly cycles. The PDMS/NMC-10 fabric possessed a SE_T value of > 20 dB in the whole X-band, satisfying the minimum
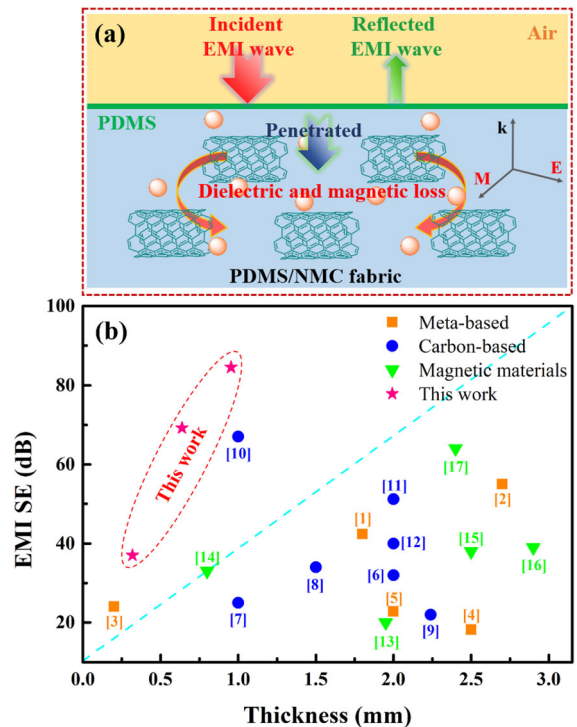
Fig. 7 **a** Schematic illustration of the EMI shielding mechanism of PDMS/NMC fabrics. **b** Comparison of the EMI SE as a function of the sample thickness, and the detailed specification of each data point was summarized in Table S2

requirement for commercial application. After 20 cycles of L-b-L assembly, the SE_T value was up to 35 dB, superior to most of reported EMI shielding materials coated with carbon-based materials(Song et al. 2015) or conductive polymers(Zhang et al. 2016). It is reasonable that the enhancement of EMI SE_T for PDMS/NMC fabrics was attributed to the continuous addition of electrical MWCNTs layers and magnetic $NiFe_2O_4$ layers. On the one hand, the increasing dipole polarization and interfacial polarization at the interfaces between MWCNTs and $NiFe_2O_4$, leaded to a linear growth in EMI shielding due to the almost same deposited mass of MWCNTs/ $NiFe_2O_4$ layer for each assembly cycle (Fig. 2i). On the other hand, the multilayer structure induced more microwave reflections at the interfaces between MWCNTs and $NiFe_2O_4$ with different permittivity and permeability, thus resulting in more electromagnetic loss. The linear dependence of EMI shielding performance with the L-b-L assembly of MWCNTs/ $NiFe_2O_4$ layer displayed the controllability of EMI SE, contributing to premeditated fabrication of EMI

shielding materials. Furthermore, it could be seen from Fig. 6d that the EMI SE was increased to $\approx$ 69 and $\approx$ 84.5 dB by laminating two and three pieces of PDMS/NMC-20 fabric (0.319 mm), which reached 'AAAAA' grade for professional use (Table S1).

To further explore the EMI shielding mechanism of PDMS/NMC fabrics, the average SE_T, SE_A and SE_R in the X-band were calculated (Fig. 6g). Apparently, SE_A was always larger than SE_R for all samples, for example, the average SE_T, SE_A and SE_R of PDMS/NMC-20 fabric reached 37.0, 25.7, and 11.3 dB, respectively, revealing the contribution from the SE_A to the SE_T (69.5%) was even larger than that of SE_R (30.5%). This finding indicated that the electromagnetic waves penetrated into this material were mainly attenuated by absorption. Figure 6h, i depicted the relationship of values of average SE_T, SE_A and SE_R and electrical-magnetic properties. Both SE_A and SE_R indicated an increased substantially behavior with increasing σ and Ms, whereas a more markedly increasement of SE_A was observed than that of SE_R, further affirming that microwave absorption was the predominant attenuation. Based on the above analysis, a feasible mechanism was proposed in Fig. 7a: when the incident electromagnetic waves attacked the surface of PDMS/NMC fabrics, a part of electromagnetic waves were directly bounced back. The remaining part penetrated into the MWCNTs/NiFe$_2$O$_4$ layer, where electromagnetic waves were attenuated by dielectric loss and magnetic loss. Meanwhile, the abundant MWCNTs/NiFe$_2$O$_4$ interfaces also facilitate the interfacial polarization and internal multiple reflections, further leading to the energy dissipation of the electromagnetic waves. As a result, the synergetic effects of dielectric loss, magnetic loss, and interfacial loss contributed to the good EMI shielding performance of PDMS/NMC fabrics.

In addition to the EMI SE, sample thickness also plays a vital role in determining the application potential for EMI shielding, the specific SE value (SSE/t, SE divided by the samples of density and thickness) therefore is a more credible parameter to evaluate the EMI shielding performance of different shields. As shown in Fig. 6g, the SSE/t value of PDMS-20 fabric reached 1382 dB cm^2 g^{-1}, which was higher than those reported shielding materials such as the Reduced Graphene Oxide/Polymer Composites (692 dB cm^2 g^{-1}) (Yan et al. 2015), and carbon foam (1250 dB cm^2 g^{-1}) (Moglie et al. 2012). For

traditional metal-based shielding materials, like silver nanowire/polyurethane nanocomposites(Zeng et al. 2017), silver-plating carbon fibers(Li et al. 2015), and fabric-supported polyaniline/cobalt-nickel coatings (Zhao et al. 2017), possess relatively high EMI shielding performance, but strong surface reflection of electromagnetic waves coupled with adding additional weight limit their applications. Recently, carbon-based EMI shielding materials and magnetic materials exhibit enchanting potential for EMI shielding due to high microwave absorption and low density, for example, Fe$_3$O$_4$@reduced graphene oxide/natural rubber composites(Zhan et al. 2018a), phthalonitrile-based carbon foam(Chen et al. 2016), and others(Kong et al. 2019; Zhang et al. 2019; Zhao et al. 2018). Nevertheless, few EMI shielding materials can integrate superior EMI SE with thin thickness. As presented in Fig. 7b, our PDMS/NMC-20 fabric with thin thicknesses ranked at the top of comparison chart and exhibited outstanding EMI shielding performance compared with most of metal-based and carbon-based shielding materials at larger thicknesses, suggesting the huge potential for applications as lightweight shielding materials.

Practical application properties

Performance stability is critical to practical applications in different environments, in this work, the electrical conductivity variation of PDMS/NMC-20 fabric were investigated by undergoing physical (washing and tape peeling) and chemical (pH and solvents) tests. The PDMS/NMC-20 fabric maintained a good electrical conductivity and EMI SE, with only less than 10% decrease after washing used commercial detergent solution for 30 cycles (Fig. 8a, Fig. S6a), and the results surpass other previous studies (Ghosh et al. 2018a, 2019a). The tape peeling test indicated that no residual particles were observed on the tape after stripping the tape away (Fig. S7), implying the good adhesion fastness between PDMS/NM layer and CF substrate. Additionally, the PDMS/NMC-20 fabric showed favorable electrical conductivity stability in almost all the solvents after immersing for 24 h, the retention rate was up to 90% in 0.1 mol/L HCl, 50 g/L NaOH and acetone (Fig. 8b, Fig. S6b). The robust performance and structural stability mainly originated from the excellent protection of external PDMS layer and strong interfacial interactions between MWCNTs
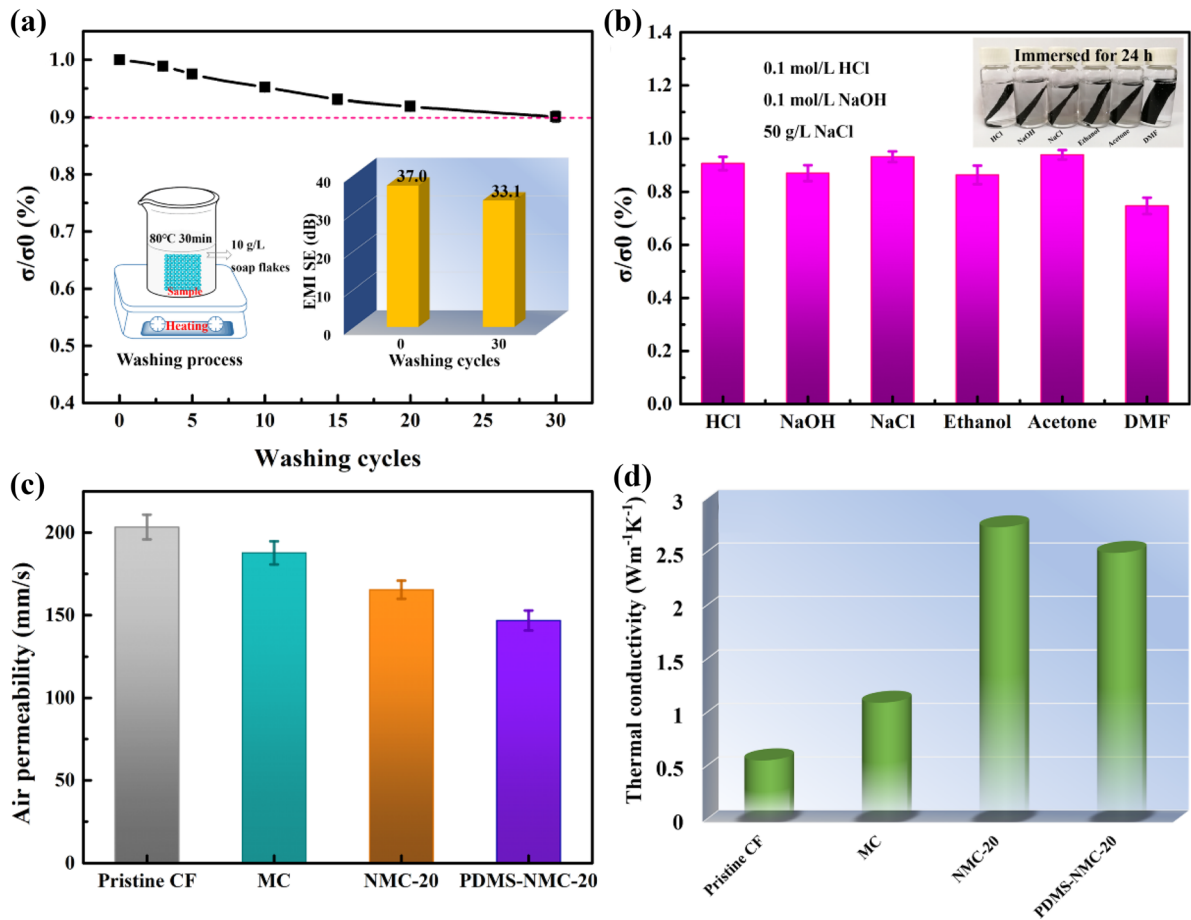
Fig. 8 The effects of **a** washing and **b** solvents on electrical conductivity of PDMS/NMC-20 fabric. **c** The air permeabilities and **d** thermal conductivity of pristine CF, MC, NMC-20, and PDMS/NMC-20

and $NiFe_2O_4$, allowing for a long-term and stable electromagnetic shielding effectiveness in real applications. Besides, the appropriate breathability and mechanical properties are also advantageous in textile field as well as EMI shielding application. Compared with pristine CF sample, the NMC-20 fabric and its PDMS-coated counterpart displayed a slight decrease in air permeability due to the blocking effect of additional deposited layer on the air voids, but still keep well-retained breathability (Fig. 8c). Table S3 indicated that the process did not significantly affect the tensile properties and flexibility of cotton fabrics.

In addition to the above significant functions, the thermal conductivity should also be taken into consideration because absorbed electromagnetic wave will converse into heat, and good heat dissipation helps to protect the electrical devices in the practical use. Figure 8d showed the thermal conductivity of composite fabrics. Evidently, the NMC-20 and PDMS-NMC-20 fabrics demonstrated an improved thermal conductivity as compared to pristine CF sample, for example, the PDMS/NMC-20 fabric possessed a high thermal conductivity of 2.52 W $m^{-1}K^{-1}$, about 4.34 times as high as that of pristine CF. The enhancing thermal conductivity could be attributed to two aspects: The L-b-L assembled MWCNTs/$NiFe_2O_4$ layers promoted the formation of effective heat conduction path; the strong interfacial adhesion interaction between P-MWCNTs and N-$NiFe_2O_4$ increased the connecting point and thus decreased the interfacial thermal resistance. Therefore, the combination of excellent EMI shielding performance, good water-resistant feature, electrical-magnetic properties, breathability, thermal

conductivity, robust structural and performance stability make the resultant fabrics applied in all parts of textiles fields-for clothing, home and technical textiles, such as protective clothing for pregnant women who want to protect fetus from EMI radiation, work clothing or tents used to prevent radar detection by the enemy, and the sophisticated electronics that need shielding shell to block the radiation interference from nearby electronic devices.

Conclusions

In summary, a flexible and durable PDMS/NMC fabric with excellent EMI shielding performance was successfully prepared by a L-b-L assembly method involving MWCNTs and $NiFe_2O_4$ alternatively followed by a PDMS coating on the external surface. Thanks to the L-b-L structure and the synergistic effect between electrical and magnetic components, the resultant PDMS/NMC-20 fabric possessed superior electrical conductivity (up to 18 S/m), high EMI SE ($\approx$ 37.0 dB for one piece and $\approx$ 85 dB for three pieces), and good thermal conductivity (2.52 W $m^{-1}K^{-1}$). Furthermore, the external PDMS layer offered a hydrophobic surface, which enhancing the long-term stability of electrical conductivity and EMI shielding efficiency in the practical use. We believe this material with such excellent features can be a good candidate applied in EMI shielding fields.

Compliance with ethical standards

Conflict of interest The authors declare no competing financial interest.

References

Cao MS, Yang J, Song W, Zhang D, Wen B, Jin H, Hou ZL, Yuan J (2012) Ferroferric oxide/multiwalled carbon nanotube vs polyaniline/ferroferric oxide/multiwalled carbon nanotube multiheterostructures for highly effective microwave absorption. Acs Appl Mater Interfaces 4:6949–6956

Cataldi P, Ceseracciu L, Athanassiou A, Bayer IS (2017) Healable cotton-graphene nanocomposite conductor for wearable electronics. ACS Appl Mater Interfaces 9:13825–13830

Chen Y, Zhang HB, Yang Y, Wang M, Cao A, Yu ZZ (2016) High-performance epoxy nanocomposites reinforced with three-dimensional carbon nanotube sponge for electromagnetic interference shielding. Adv Funct Mater 26:447–455

Cui CH, Yan DX, Pang H, Jia LC, Xu X, Yang S, Xu JZ, Li ZM (2017) A high heat-resistance bioplastic foam with efficient electromagnetic interference shielding. Chem Eng J 323:29–36

Ghosh S, Mondal S, Ganguly S, Remanan S, Singha N, Das NC (2018a) Carbon nanostructures based mechanically robust conducting cotton fabric for improved electromagnetic interference shielding. Fiber Polym 19:1064–1073

Ghosh S, Remanan S, Mondal S, Ganguly S, Das P, Singha N, Das NC (2018b) An approach to prepare mechanically robust full IPN strengthened conductive cotton fabric for high strain tolerant electromagnetic interference shielding. Chem Eng J 344:138–154

Ghosh S, Ganguly S, Das P, Das TK, Bose M, Singha NK, Das AK, Das NC (2019a) Fabrication of reduced graphene oxide/silver nanoparticles decorated conductive cotton fabric for high performing electromagnetic interference shielding and antibacterial application. Fiber Polym 20:1161–1171

Ghosh S, Ganguly S, Remanan S, Das NC (2019b) Fabrication and investigation of 3D tuned PEG/PEDOT: PSS treated conductive and durable cotton fabric for superior electrical conductivity and flexible electromagnetic interference shielding. Compos Sci Technol 181:107682

González M, Baselga J, Pozuelo J (2019) Modulating the electromagnetic shielding mechanisms by thermal treatment of high porosity graphene aerogels. Carbon 147:27–34

Hang Z, Lei H, Lu Y (2016) Electromagnetic shielding effectiveness and serviceability of the multilayer structured cuprammonium fabric/polypyrrole/copper (CF/PPy/Cu) composite. Chem Eng J 297:170–179

He P, Wang XX, Cai YZ, Shu JC, Zhao QL, Yuan J, Cao MS (2019) Tailoring $Ti_3C_2T_x$ nanosheets to tune local conductive network as an environmentally friendly material for highly efficient electromagnetic interference shielding. Nanoscale 11:6080–6088

Hsiao ST, Ma CM, Liao WH, Wang YS, Li SM, Huang YC, Yang RB, Liang WF (2014) Lightweight and flexible reduced graphene oxide/water-borne polyurethane composites with high electrical conductivity and excellent electromagnetic interference shielding performance. ACS Appl Mater Interfaces 6:10667–10678

Huang G, Liu L, Wang R, Zhang J, Sun X, Peng H (2016) Smart color-changing textile with high contrast based on a single-sided conductive fabric. J Mater Chem C 4:7589–7594

Jia L-C, Xu L, Ren F, Ren P-G, Yan D-X, Li Z-M (2019) Stretchable and durable conductive fabric for ultrahigh performance electromagnetic interference shielding. Carbon 144:101–108

Jiao Q, Wang Y, Liang H, Li H, Yun Z (2016) Synthesis of magnetic nickel ferrite microspheres and their microwave absorbing properties. Chem Res Chinese Univ 32:678–681

Kong L, Yin X, Xu H, Yuan X, Wang T, Xu Z, Huang j, Yang R, Fan H (2019) Powerful absorbing and lightweight

electromagnetic shielding CNTs/RGO composite. Carbon 145:61–66

Li J, Qi S, Zhang M, Wang Z (2015) Thermal conductivity and electromagnetic shielding effectiveness of composites based on Ag-plating carbon fiber and epoxy. J Appl Polym Sci 132:42306

Li J, Xie Y, Lu W, Chou TW (2018) Flexible electromagnetic wave absorbing composite based on 3D rGO-CNT-Fe_3O_4 ternary films. Carbon 129:76–84

Liu Y, Jiang H, Zhu Y, Yang X, Li C (2016) Transition metals (Fe, Co, and Ni) encapsulated in nitrogen-doped carbon nanotubes as bi-functional catalysts for oxygen electrode reactions. J Mater Chem A 4:1694–1701

Liu M, Pu X, Jiang C, Liu T, Huang X, Chen L, Du C, Sun J, Hu W, Wang Z (2017a) Large-area all-textile pressure sensors for monitoring human motion and physiological signals. Adv Mater 29:1303700

Liu C, Ye X, Wang X, Liao X, Huang X, Shi B (2017b) Collagen fiber membrane as an absorptive substrate to coat with carbon nanotubes-encapsulated metal nanoparticles for lightweight, wearable, and absorption-dominated shielding membrane. Ind Eng Chem Res 56:8553–8562

Liu J, Liu Y, Zhang H-B, Dai Y, Liu Z, Yu Z-Z (2018a) Superelastic and multifunctional graphene-based aerogels by interfacial reinforcement with graphitized carbon at high temperatures. Carbon 132:95–103

Liu J, Zhang HB, Xie X, Yang R, Liu Z, Liu Y, Yu ZZ (2018b) Multifunctional, superelastic, and lightweight MXene/polyimide aerogels. Small 14:e1802479

Lv P, Wei A, Wang Y, Li D, Zhang J, Lucia LA, Wei Q (2016) Copper nanoparticles-sputtered bacterial cellulose nanocomposites displaying enhanced electromagnetic shielding, thermal, conduction, and mechanical properties. Cellulose 23:3117–3127

Moglie F, Micheli D, Laurenzi S, Marchetti M, Mariani Primiani V (2012) Electromagnetic shielding performance of carbon foams. Carbon 50:1972–1980

Ren F, Song D, Li Z, Jia L, Zhao Y, Yan D, Ren P (2018) Synergistic effect of graphene nanosheets and carbonyl iron–nickel alloy hybrid filler on electromagnetic interference shielding and thermal conductivity of cyanate ester composites. J Mater Chem C 6:1476–1486

Shahzad F, Alhabeb M, Hatter CB, Anasori B, Man HS, Koo CM, Gogotsi Y (2016) Electromagnetic interference shielding with 2D transition metal carbides (MXenes). Science 353:1137–1140

Song WL, Guan XT, Fan LZ, Cao WQ, Wang CY, Zhao QL, Cao MS (2015) Magnetic and conductive graphene papers toward thin layers of effective electromagnetic shielding. J Mater Chem A 3:2097–2107

Varshney S, Ohlan A, Jain VK, Dutta VP, Dhawan SK (2014) In situ synthesis of polypyrrole-γ-Fe_2O_3-fly ash nanocomposites for protection against EMI pollution. Ind Eng Chem Res 53:14282–14290

Wang Y, Wang W, Yu D (2017) Three-phase heterostructures f-$NiFe_2O_4$/PANI/PI EMI shielding fabric with high microwave absorption performance. Appl Sur Sci 425:518–525

Wang L, Qiu H, Liang C, Song P, Han Y, Gu J, Kong J, Pan D, Guo Z (2019a) Electromagnetic interference shielding MWCNT-Fe_3O_4@Ag/epoxy nanocomposites with

satisfactory thermal conductivity and high thermal stability. Carbon 141:506–514

Wang QW, Zhang HB, Liu J, Zhao S, Xie X, Liu X, Yang R, Koratkar N, Yu ZZ (2019b) Multifunctional and water-resistant MXene-decorated polyester textiles with outstanding electromagnetic interference shielding and joule heating performances. Adv Funct Mater 29:1806819

Weng GM, Li J, Alhabed M, Karpovich C, Wang H, Lipton J, Maleski K, Kong J, Shaulsky E, Elimelech M, Gogotsi Y, Taylor A (2018) Layer-by-layer assembly of cross-functional semi-transparent MXene-carbon nanotubes composite films for next-generation electromagnetic interference shielding. Adv Funct Mater 28:1803360

Xu Y, Yang Y, Yan DX, Duan H, Zhao G, Liu Y (2019) Flexible and conductive polyurethane composites for electromagnetic shielding and printable circuit. Chem Eng J 360:1427–1436

Yan DX, Pang H, Li B, Vajtai R, Xu L, Ren PG, Wang JH, Li ZM (2015) Structured reduced graphene oxide/polymer composites for ultra-efficient electromagnetic interference shielding. Adv Funct Mater 25:559–566

Yang Y, Li M, Wu Y, Wang T, Choo ESG, Ding J, Zong B, Yang Z, Xue J (2016) Nanoscaled self-alignment of Fe_3O_4 nanodiscs in ultrathin rGO films with engineered conductivity for electromagnetic interference shielding. Nanoscale 8:15989–15998

Zeng Z, Chen M, Pei Y, Seyed Shahabadi SI, Che B, Wang P, Lu X (2017) Ultralight and flexible polyurethane/silver nanowire nanocomposites with unidirectional pores for highly effective electromagnetic shielding. ACS Appl Mater Interfaces 9:32211–32219

Zhan Y, Wang J, Zhang K, Li Y, Meng Y, Yan N, Wei W, Peng F, Xia H (2018a) Fabrication of a flexible electromagnetic interference shielding Fe_3O_4@reduced graphene oxide/natural rubber composite with segregated network. Chem Eng J 344:184–193

Zhan Y, Wang J, Zhang K, Li Y, Meng Y, Yan N, Wei W, Peng F, Xia H (2018b) Fabrication of a flexible electromagnetic interference shielding Fe_3O_4@reduced graphene oxide/natural rubber composite with segregated network. Chem Eng J 344:184–193

Zhang Y, Qiu M, Yu Y, Wen B, Cheng L (2016) A novel polyaniline-coated bagasse fiber composite with core-shell heterostructure provides effective electromagnetic shielding performance. ACS Appl Mater Interfaces 9:809–818

Zhang Y, Zhang H-B, Wu X, Deng Z, Zhou E, Yu ZZ (2019) Nanolayered cobalt@carbon hybrids derived from metal-organic frameworks for microwave absorption. ACS Appl Nano Mater 2:2325–2335

Zhao H, Hou L, Bi S, Lu Y (2017) Enhanced X-band electromagnetic-interference shielding performance of layer-structured fabric-supported polyaniline/cobalt-nickel coatings. ACS Appl Mater Interfaces 9:33059–33070

Zhao S, Zhang HB, Luo JQ, Wang QW, Xu B, Hong S, Yu ZZ (2018) Highly electrically conductive three-dimensional $Ti_3C_2T_x$ MXene/reduced graphene oxide hybrid aerogels with excellent electromagnetic interference shielding performances. ACS Nano 12:11193–11202

Zhou E, Xi J, Guo Y, Liu Y, Xu Z, Gao W, Ying J, Chen Z, Gao C (2018) Synergistic effect of graphene and carbon

nanotube for high-performance electromagnetic interference shielding films. Carbon 133:316–322

Zhu S, Xing C, Wu F, Zuo X, Zhang Y, Yu C, Chen M, Li W, Li Q, Liu L (2019) Cake-like flexible carbon nanotubes/graphene composite prepared via a facile method for high-performance electromagnetic interference shielding. Carbon 145:259–265

Zou L, Zhang S, Li X, Lan C, Qiu Y, Ma Y (2016) Step-by-step strategy for constructing multilayer structured coatings toward high-efficiency electromagnetic interference shielding. Adv Mater Interfaces 3:1500476